

Article

Porous Pb-Doped ZnO Nanobelts with Enriched Oxygen Vacancies: Preparation and Their Chemiresistive Sensing Performance

Kai-Ge Zheng^{1,2}, Tian-Yu Yang^{1,2} and Zheng Guo^{1,2,*} 

¹ Information Materials and Intelligent Sensing Laboratory of Anhui Province, Institutes of Physical Science and Information Technology, Anhui University, Hefei 230601, China; q19201115@stu.ahu.edu.cn (K.-G.Z.); q21201024@stu.ahu.edu.cn (T.-Y.Y.)

² Key Laboratory of Structure and Functional Regulation of Hybrid Materials (Anhui University), Ministry of Education, Hefei 230601, China

* Correspondence: zhguo@ahu.edu.cn

Abstract: Among various approaches to improve the sensing performance of metal oxide, the metal-doped method is perceived as effective, and has received great attention and is widely investigated. However, it is still a challenge to construct heterogeneous metal-doped metal oxide with an excellent sensing performance. In the present study, porous Pb-doped ZnO nanobelts were prepared by a simple partial cation exchange method, followed by in situ thermal oxidation. Detailed characterization confirmed that Pb was uniformly distributed on porous nanobelts. Additionally, it occupied the Zn situation, not forming its oxides. The gas-sensing measurements revealed that 0.61 at% Pb-doped ZnO porous nanobelts exhibited a selectively enhanced response with long-term stability toward n-butanol among the investigated VOCs. The relative response to 50 ppm of n-butanol was up to 47.7 at the working temperature of 300 °C. Additionally, the response time was short (about 5 s). These results were mainly ascribed to the porous nanostructure, two-dimensional belt-like morphology, enriched oxygen vacancies and the specific synergistic effect from the Pb dopant. Finally, a possible sensing mechanism of porous Pb-doped ZnO nanobelts is proposed and discussed.

Keywords: zinc oxide; lead doping; partial cation exchange reaction; n-butanol; gas sensing



Citation: Zheng, K.-G.; Yang, T.-Y.; Guo, Z. Porous Pb-Doped ZnO Nanobelts with Enriched Oxygen Vacancies: Preparation and Their Chemiresistive Sensing Performance. *Chemosensors* **2022**, *10*, 96. <https://doi.org/10.3390/chemosensors10030096>

Academic Editor: Andrea Ponzoni

Received: 21 January 2022

Accepted: 24 February 2022

Published: 1 March 2022

Publisher's Note: MDPI stays neutral with regard to jurisdictional claims in published maps and institutional affiliations.



Copyright: © 2022 by the authors. Licensee MDPI, Basel, Switzerland. This article is an open access article distributed under the terms and conditions of the Creative Commons Attribution (CC BY) license (<https://creativecommons.org/licenses/by/4.0/>).

1. Introduction

Due to the outstanding merits of low cost, easy fabrication, high-sensing performance and compatibility with modern electronic devices, resistive-type metal oxide semiconductor (MOS) gas sensors have been widely applied to detect VOCs in various fields, such as human health, environment monitoring, food processing and industrial manufacture. Compared with p-type oxide semiconductors, n-type oxide semiconductors have received more attention since the discovery of oxide semiconductor-based gas sensors in the 1960s, because of their special sensing mechanism and highly relative response [1–4]. Among the n-type MOSs, ZnO as a typical one has been widely applied and investigated in gas sensors because of its high electron mobility, non-toxicity, good stability and simple synthesis route [5]. However, the property of pure ZnO was not satisfied, resulting in the need to improve the intrinsic performance through many ingenious methods, depending on the practical situation of application for further eliminating false-positive or interfering signals and simplifying the design of electronic nose system.

Numerous diverse systematic researches showed that the key sensing parameters of resistive-type MOS gas sensors could be enhanced by the composite with other MOSs, resulting in a controlled chemical affinity toward a specific gas, modified acid-base properties and the tuned catalytic activity [6]. The technology of doping ions in MOSs was also widely applied in the practical field of improving performance, which was responsible for forming oxygen vacancies and changing electronic structures of metal oxides [7].

Oxygen vacancies were one of the intrinsic defects existing in the actual semiconductor samples and provided an effect similar to n-type dopants. Importantly, they increased negatively charged oxygen ions on the surface by their surrounding electron-deficient region. Meanwhile, the doping method primarily affected the shift of the Fermi level and the positions of the energy band, which could remarkably ameliorate the performance of MOSs by altering the energy band [8]. Recently, lead (Pb) doping was used in many application areas of semiconductors, due to its larger ionic radius and specific catalytic activity, which causes the relaxing of tensile strain and an improvement to the sensitization performance [9]. Furthermore, the desirable attributes brought by the doping of Pb ions included a good working stability at a high temperature (due to the high atomic number and stability of Pb), a high resistivity to decrease the baseline current of the sensors (favorable for enhancing the response) and an abundant availability in nature [10]. In addition, the desirable morphologies and structures of sensing materials were also the key points in the improvement of the sensing performance. Among them, the low-dimensional nanomaterial and porous structure were generally applied to practical gas-sensing, because the increased specific surface area always meant a larger resistance variation of sensing materials and more efficient reactions at the surface [11,12].

Herein, Pb-doped ZnO porous nanobelts, owing to their great crystal form and uniformly two-dimensional porous nanostructures, were successfully synthesized via a simply partial cation exchange method with in situ thermal oxidation. Different amounts of Pb-doped ZnO were carefully prepared and, subsequently, the ZnO porous nanobelts with optimal amounts of Pb were systematically explored in relation to their gas-sensing performance to n-butanol. The synthetic strategy presented here could be generally extended to design other semiconductor metal oxide gas sensors with outstanding performances.

2. Experimental Section

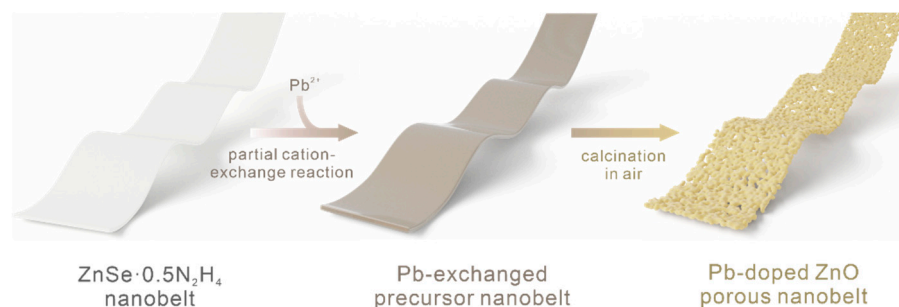
2.1. Chemical Reagents

Analytical grade ethanol, ethylene glycol (EG), $\text{N}_2\text{H}_4 \cdot \text{H}_2\text{O}$ (mass fraction of N_2H_4 , 85%), polyvinylpyrrolidone (PVP, K30), Se powders, ZnCl_2 and $\text{Pb}(\text{NO}_3)_2$ were purchased from Shanghai Chemical Reagent Co., Ltd. (Shanghai, China) without further purification. Milli-Q water with a resistivity of 18.25 M Ω cm was used in the preparation of aqueous solutions.

2.2. Preparation of Pb-Doped ZnO Porous Nanobelts

The whole preparation process is demonstrated in Scheme 1. $\text{ZnSe} \cdot 0.5\text{N}_2\text{H}_4$ precursor nanobelts were firstly synthesized as subsequent templates via a convenient hydrothermal method that was reported in our previous reports [13,14]. In a typical synthetic process, a brown homogeneous solution is formed by the dissolution of 0.4 mmol Se powder into 20 mL of aqueous $\text{N}_2\text{H}_4 \cdot \text{H}_2\text{O}$. Then, the ZnCl_2 aqueous solution, which was prepared using 0.2 mmol of ZnCl_2 and 20 mL of deionized water, was added, drop by drop, to the above brown homogeneous solution under vigorous magnetic stirring. After stirring for about 1 h, the obtained solution was transferred into a 50 mL Teflon-lined stainless steel autoclave and put into an oven at 180 °C. After 12 h, the autoclave was cooled down to room temperature naturally. Finally, the precursor of $\text{ZnSe} \cdot 0.5\text{N}_2\text{H}_4$ nanobelts was obtained by washing them several times with distilled water. Then, the achieved precursor nanobelts were all dispersed into a 20 mL EG solution containing 0.1 g of poly(vinylpyrrolidone) (PVP, K30). Afterwards, a 5 mL EG solution with a certain amount of $\text{Pb}(\text{NO}_3)_2$ was added, drop by drop, into the homogenous solution. After continuously stirring for 2 h, a dark color uniform solution was formed. Subsequently, the solution was transferred into a 50 mL Teflon-lined stainless steel autoclave and was placed into an oven at 70 °C for 12 h. Finally, the dark green Pb-doped precursor nanobelts were achieved after washing and centrifuging with ethanol and distilled water several times to remove the excess impurities. Through manipulating the added amount of $\text{Pb}(\text{NO}_3)_2$ (0.001 mmol, 0.002 mmol, 0.004 mmol and 0.006 mmol), the actual doped ratios of 0.44 at%, 0.61 at%, 1.39 at% and 2.01 at% were

achieved and identified by XPS. In the following, the as-prepared samples were thermally oxidized in air. Referring to the thermogravimetric analysis of our previous report [15], the samples were firstly heated at a low heating rate of 2 °C/min to 350 °C and maintained for 30 min to totally remove the hydrazine ligand. The temperature was continuously increased to 500 °C at the heating rate of 1 °C/min, for a better crystal structure and morphology in the oxidation process of the doped nanobelts and kept for 30 min. Then, the cooling process was also slow at the rate of 2 °C/min to 100 °C to maintain the characteristic structure of the samples. Finally, after naturally cooling down to room temperature, porous Pb-doped ZnO porous nanobelts were achieved.



Scheme 1. Synthetic process of porous Pb-doped ZnO nanobelts.

2.3. Fabrication and Measurements of Gas-Sensing Devices

An assembly technique combined with in situ calcination was employed to fabricate the gas-sensing devices with a stable and uniform sensing film of Pb-doped ZnO porous nanobelts. As shown in Figure S1a, the square alumina ceramic slices (3 mm × 3 mm × 0.25 mm, length × width × thickness) with a pair of Au electrodes with a 0.3 mm gap on the front side and an Ru-based thick film resistor on the back side were set as the test substrates. The effective area of the sensing film was about 0.42 mm². Firstly, a homogeneous solution was formed by dispersing a small amount of the as-prepared Pb-exchanged precursor nanobelts in moderate ethanol and dropped on the front side of the alumina ceramic slice to form a thin film. After this was repeated several times, the front side with the Au electrodes was covered with a dense and uniform Pb-exchanged precursor nanobelt film. Then, they were in situ transformed on the surface of the alumina ceramic slices into a uniform Pb-doped porous ZnO nanobelt sensing film following the above-mentioned thermal oxidation approach.

The sensing measurement of the Pb-doped ZnO porous nanobelts was performed in a homemade gas sensor testing system, as shown in Figure S1b, including a Keithley 6487 picoammeter/voltage sourcemeter, connecting with two Au electrodes to act as both the current reader and voltage source; a heating voltage modulator was employed to offer the working temperature of the sensor by applying a specific voltage on the Ru-based thick film resistor. All gas-sensing measurements were performed in dry air and the certain concentration gas to be tested was injected by a minitype syringe. The relative response of the fabricated gas sensors was defined as $S = R_a/R_g$, where R_a is the resistance of the sensing film in dry air and R_g is the resistance in dry air containing the detected gases. Furthermore, the response time (t_{res}) and recovery time (t_{rec}) were defined as the times required to reach 90% of the final equilibrium value, respectively.

2.4. Characterization

X-ray photoelectron spectroscopy (XPS) analyses of the samples was conducted on a Thermo Scientific ESCALAB Xi+ X-ray Photoelectron Spectrometer microprobe (Thermo ESCALAB 250Xi, Waltham, MA, USA). The energy scale was internally calibrated by referencing the binding energy (E_b) of the C 1s peak at 284.60 eV for contaminated carbon. The microstructure and morphology of the as-prepared samples were characterized by transmission electron microscopy (TEM, Tecnai TF-20, 200 kV) and field-emission scanning

electron microscopy (FESEM, Quanta 200 FEG, FEI Company, Hillsboro, OR, USA). The crystal components and structures were determined with an X-ray power diffractometer (smart Lab 9KW) using Cu K α radiation (radiation $\lambda = 1.5418 \text{ \AA}$).

3. Results and Discussion

3.1. Preparation and Characterization of the Pb-Doped ZnO Porous Nanobelts

The morphologies of all the achieved nanobelts were first investigated by SEM, as shown in Figure 1. The as-prepared precursors of ZnSe \cdot 0.5N $_2$ H $_4$ in Figure 1a can be identified as homogeneous nanobelts with a relatively large length–width ratio and smooth surface. After being exchanged with 0.61 at% Pb $^{2+}$ cations, their morphologies, displayed in Figure 1b, are still maintained without any protrusions or other obviously heterogeneous areas. After calcination in air, they are all transformed into a belt-like porous nanostructure, which can be seen in Figure 1c,d, respectively. This morphological evolution is caused by the removal of the N $_2$ H $_4$ ligand and the oxidation of the Se element following subsequent sublimation at a high temperature. For Pb $^{2+}$ -exchanged precursor nanobelts, the corresponding formed product was a porous Pb-doped ZnO nanobelt. Furthermore, the precursor exchanged with other amounts of Pb $^{2+}$ cations and their corresponding annealed products were also investigated and a similar phenomenon was also observed, as shown in Figure S2.

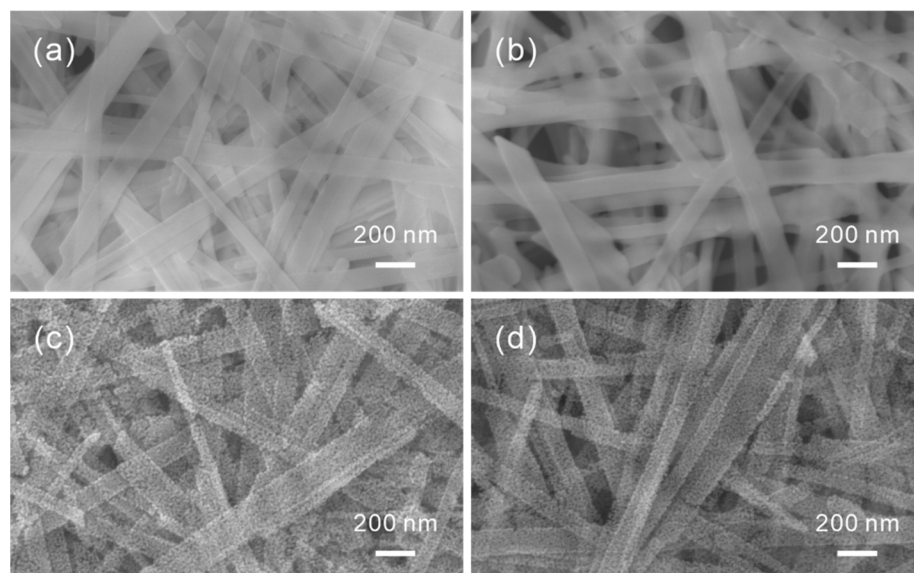


Figure 1. SEM images of ZnSe \cdot 0.5N $_2$ H $_4$ precursor nanobelts before (a) and after (c) thermal oxidation, and 0.61 at% Pb-exchanged ZnSe \cdot 0.5N $_2$ H $_4$ nanobelts before (b) and after (d) thermal oxidation.

To illuminate the microstructure of the as-prepared Pb $^{2+}$ -exchanged precursor nanobelts before and after calcination in air, the characterization of their TEMs was performed. Similar to the ZnSe \cdot 0.5N $_2$ H $_4$ precursor nanobelts, the Pb $^{2+}$ -exchanged precursor nanobelts are also not stable and easily decomposed under the high-power electron beam. This phenomenon can be seen from TEM images shown in Figure S3a,b. Notably, after the exchange with Pb $^{2+}$ cations, the achieved nanobelts are uniformly distributed with the Pb element in addition to Zn and Se elements, which can be seen from the elemental mapping shown in Figure S3c–f. From the typical TEM image of a single nanobelt shown in Figure 2a, the as-prepared porous Pb-doped ZnO nanobelts are constructed by numerous interconnected nanocrystal grains with spontaneously generated micropores and nanopores. Evidently, this special nanostructure is favorable for the diffusion of gas molecules, resulting in an enhanced gas-sensing performance. Further crystal information of the Pb-doped ZnO porous nanobelt was confirmed by the high-resolution TEM image in Figure 2b, in which the lattice fringes can clearly be observed with a lattice spacing of 0.247 nm and 0.281 nm,

corresponding to the (101) and (100) planes of hexagonal zinc oxide, respectively, with no other crystalline phases. The compositional elemental mapping patterns of Zn, Pb and O in the high-angle annular dark field (HAADF) image of the Pb-doped ZnO porous nanobelt in Figure 2c are displayed in Figure 2d–f, revealing that they are uniformly distributed along the nanobelt. From the EDX spectrum of the obtained Pb-doped ZnO porous nanobelts shown in Figure S4, weak Pb peaks are observed in addition to the strong peaks of Zn and O. The Cu peak most likely originates from the Cu grid.

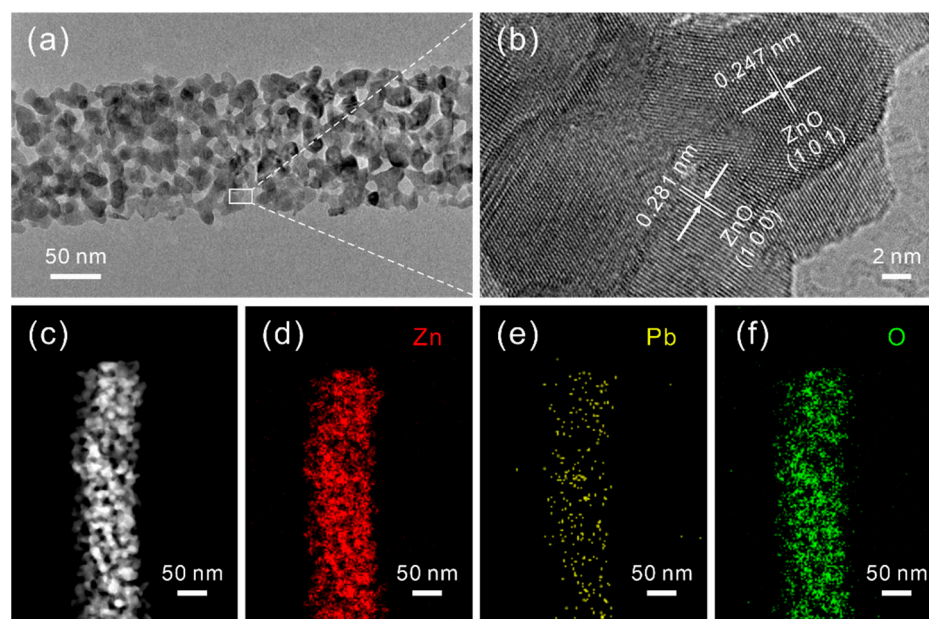


Figure 2. (a) TEM image of a single Pb-doped ZnO porous nanobelt, (b) its HRTEM image corresponds to the marked area, (c) its HAADF image and the corresponding elemental mapping patterns of (d) Zn, (e) Pb and (f) O.

Afterwards, their crystal structures were examined by XRD measurements and all intensities of the peaks were normalized. As shown in Figure 3a, clearly all emerged diffraction peaks of the above-mentioned samples are completely indexed to a hexagonal wurtzite ZnO phase (JCPDS#36-1451) without observing any diffraction peaks related to the Pb compound or other crystalline phases [16]. Additionally, the (100) diffraction peak of ZnO located at the high-resolution XRD patterns shifted with the addition of Pb, as presented in Figure 3b. By increasing the doped amount of Pb, the position of the (100) diffraction peaks shifted to lower angles. This phenomenon confirms that the Pb element, identified as Pb^{2+} by the following XPS analysis, was indeed incorporated into the ZnO lattice and occupied the hexagonal Zn^{2+} cation site [17]. Further lattice refinement of the XRD data displayed in Table S1 revealed the detailed change of their crystal lattices. Calculated by Bragg's law ($n\lambda = 2d\sin\theta$), the interplanar distance (d) values belonging to (100) peaks increase with the raising of Pb concentration, and the lattice parameters (a , c) are similarly expanded. This result is mainly caused by the larger ionic radii of Pb^{2+} (0.119 nm) compared with Zn^{2+} (0.074 nm) [18,19]. It implies the successful substitution of Pb ions for Zn ions, which is consistent with the previous reports [20,21].

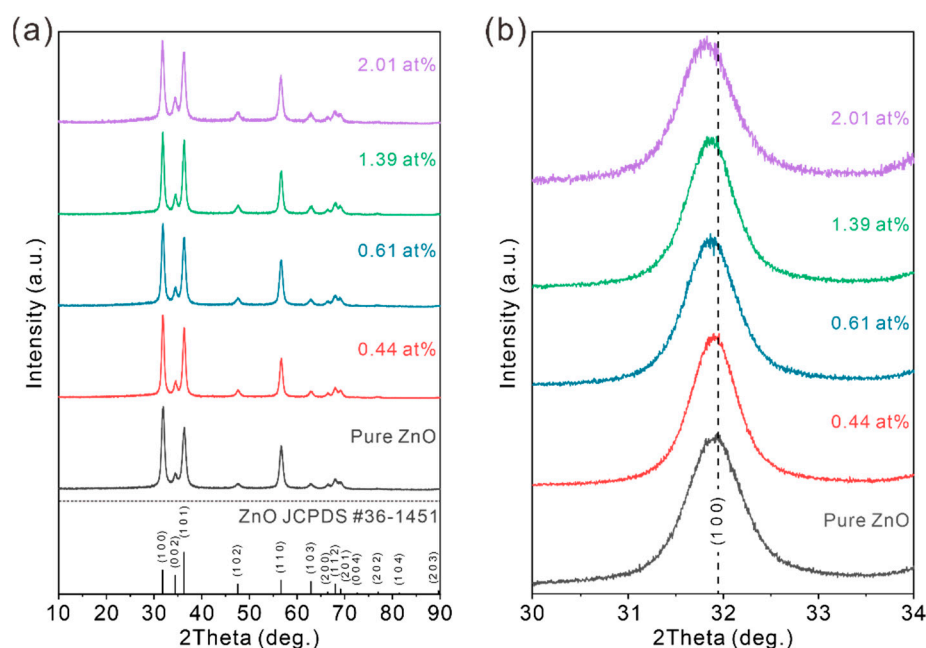


Figure 3. (a) XRD patterns of the as-prepared pure ZnO and 0.44 at%, 0.61 at%, 1.39 at% and 2.01 at% Pb-doped ZnO, and (b) their corresponding high-resolution XRD patterns at the main diffraction peak of (100).

The composition and chemical states of the as-prepared Pb^{2+} -exchanged precursor nanobelts before and after calcination in air were further investigated by XPS measurements. As the survey spectra shows in Figure 4a, the evident peaks are marked with their corresponding energy level [22]. It identifies the presence of Zn, Se and N elements before calcination and the absence of Se and N elements after calcination, regardless of whether the $\text{ZnSe}\cdot 0.5\text{N}_2\text{H}_4$ precursor nanobelts were exchanged with Pb or not. This result is ascribed to the total oxidation of the selenide and the entire removal of the hydrazine ligand. However, it is difficult to find the distinct peak of Pb, which is due to the relatively low concentration of Pb^{2+} cation in samples III and IV. Therefore, the high-resolution XPS spectra of Pb 4f in 0.61 at% Pb-doped ZnO porous nanobelts is illustrated in Figure 4b. The two peaks at about 138.71 eV and 143.45 eV, of which the peak area ratio was approximately 4:3, were observed and assigned as Pb 4f_{7/2} and Pb 4f_{5/2} orbitals, respectively [23]. It exactly matches the previous report, concerning other possible valence states, such as PbO_2 and Pb_3O_4 [24–26]. Meanwhile, the peak located here at about 139.56 eV is recognized as Zn 3s, presenting a high intensity because of the large atomic ratio between the Zn and Pb elements [27]. As shown in Figure 4c, the high-resolution Zn 2p XPS spectra of 0.61 at% Pb-doped ZnO porous nanobelts revealed that two distinct peaks at 1044.12 eV and 1021.1 eV were attributed to Zn 2p_{1/2} and Zn 2p_{3/2}, respectively [28]. Compared with the pure ZnO porous nanobelts displayed in Figure S5, the two characteristic peaks were clearly shifted 0.3 eV to high bond locations after doping with Pb due to the special electronegativity and effective charge movement between the two ions. This illustrates that the band structure of ZnO was affected by the introduction of the dopant of Pb [29]. Figure 4d displays the high-resolution O 1s XPS spectra of 0.61 at% Pb-doped ZnO porous nanobelts. Here, its peak can be deconvoluted into four types of peaks: the peak of lattice O of ZnO (O_{Zn}) at around 530.2 eV, the peak situated at 530.37 eV represents the lattice O of PbO (O_{Pb}), the peak located at around 530.66 eV attributed to the oxygen vacancy (O_{va}), and the peak at a binding energy of 531.68 eV assigned to the adsorbed oxygen (O_{ad}) [30]. The similar analysis procedure of deconvolution and fitting was also applied to the high-resolution O 1s XPS spectra of pure ZnO porous nanobelts in Figure 4e. The ratios of the different kinds of oxygen species previously stated, and their position of binding energy, are listed in Table S2. It should be noted that the corresponding characteristic peaks also have some

the gas molecules did not have enough energy to overcome the energy barrier to react with the oxygen species adsorbed on the materials surface, and the diffusion process was slow. Correspondingly, increasing the working temperature could provide extra energy to boost the reaction between the tested gas molecules and the adsorbed oxygen species. However, more was not always better. Overmuch energy from further increasing the working temperature made the gas molecules so active that they would escape from the surface of the sensing materials before the sensing process; neither were the sensing materials in a stable condition for the reaction. Meanwhile, the sensing response would also be affected by the ion doping as well as the working temperature [35]. With the increased dopants of Pb, more oxygen vacancies were formed, suggesting that more VOC molecules can be easily absorbed and activated on the surface of porous nanobelts. Hence, the sensing performance was enhanced. The 0.61% Pb-doped ZnO exhibited the best response at the working temperature of 300 °C. When its doped amount was large, the excess Pb ions occupied the active sites on the surface of the sensing materials, which is disadvantageous for the gas adsorption and causes the degradation of the gas sensing response. The optimal working temperature was at 300 °C for the Pb-doped ZnO nanobelts, which is lower than 400 °C of the optimal value for pure ZnO porous nanobelts. Hence, the 0.61% doped amount and the operating temperature of 300 °C were selected as the optimal test conditions, where the highest response of 47.7 was obtained toward 50 ppm of n-butanol. Figure 5b illustrates the real-time response curves to 50 ppm n-butanol. The corresponding resistance response curve is shown in Figure S7a. Evidently, the response time is short (about 5 s) due to their porous structures, which is favorable for the diffusion of gas molecules. The recovery time of 108 s was relatively long compared with the response time, due to the special sensing mechanism of the chemical reaction between adsorbed oxygen species and C–H bonds at surfaces of most MOS materials [36]. The more alkyl groups $(-\text{CH}_2-)_n$ a VOC molecule owned, the more gaseous products were produced during the sensing process at the surface of the sensing materials. Therefore, the time for their desorption should be longer [37].

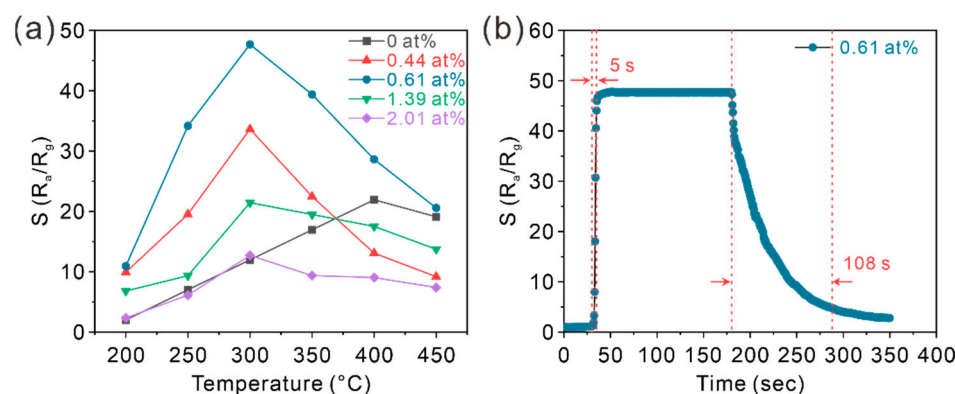


Figure 5. (a) The relative response of porous ZnO nanobelts doped with different amounts of Pb toward 50 ppm of n-butanol at different working temperatures. (b) The real-time response curve of 0.61 at% Pb-doped ZnO porous nanobelts toward 50 ppm of n-butanol at 300 °C.

Furthermore, the 0.61 at% Pb-doped ZnO and ZnO porous nanobelts were investigated in a wide concentration range of n-butanol, ranging from 1 ppm to 50 ppm at the optimal working temperature of 300 °C, and their real-time response curves are presented in Figure 6a, and its resistance curve is shown in Figure S7b. The results show a fast response of the sensors and a stable value of response in the saturation region, which has a regular relationship with the concentration of n-butanol. The relative response increased with increasing the concentration of n-butanol. A good reversibility could also be demonstrated from the fact that the resistance of the sensors was able to recover to the baseline value. Moreover, 0.61 at% Pb-doped ZnO porous nanobelts demonstrated a distinctly improved response at every point of concentration compared with pure ZnO nanobelts, which was over 4-fold at 50 ppm. The above results are linearly fitted in Figure 6b. It can be seen

that the gas sensors fabricated with 0.61 at% Pb-doped ZnO porous nanobelts displayed a higher relative response with a wide detection range than that of pure ZnO porous nanobelts. Furthermore, as seen in Table S3 [38–51], compared with previously reported n-butanol sensors based on various semiconductor nanomaterials, the fabricated sensor showed a relatively better sensing performance.

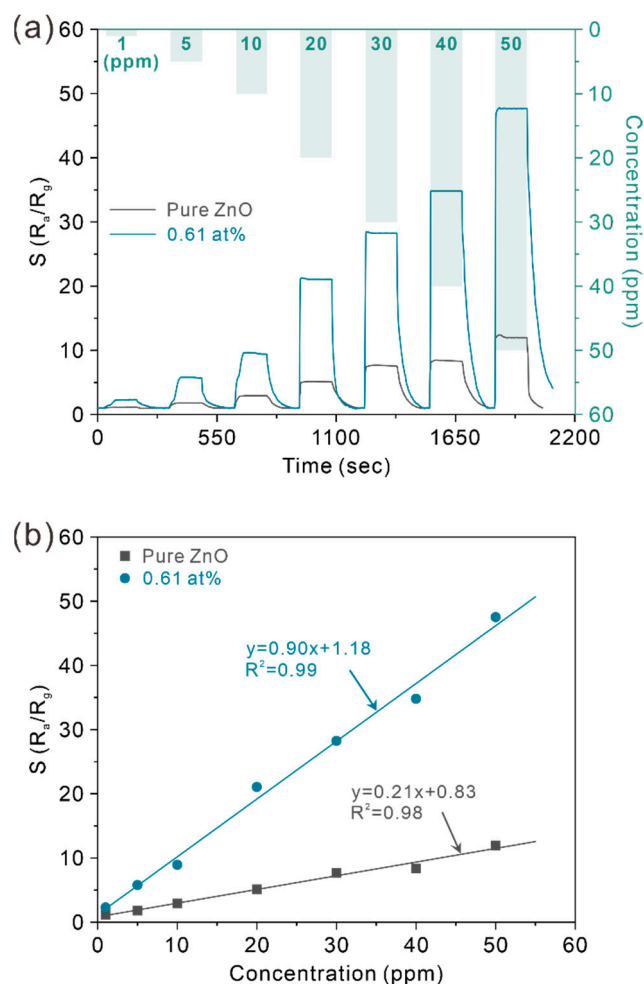


Figure 6. (a) The real-time response curves of pure ZnO porous nanobelts and 0.61 at% Pb-doped ZnO porous nanobelts toward different concentrations of n-butanol at 300 °C, and (b) their linear fitting curves between the relative responses and concentrations of n-butanol.

To investigate the relative selectivity of the sensor fabricated with 0.61 at% Pb-doped ZnO porous nanobelts, nine kinds of typical VOCs (m-xylene, ethanol, formaldehyde, n-butanol, acetone, benzene, isopropanol, methanol and diethyl ether) were explored at the same concentration of 50 ppm. As shown in Figure 7a, the results reveal that the 0.61 at% Pb-doped ZnO porous nanobelts exhibited a high response of 47.7 to n-butanol, a noticeable response of 34.3 to isopropanol, but significantly reduced responses toward other tested VOCs. Compared with pristine ZnO porous nanobelts, 0.61 at% Pb-doped ZnO porous nanobelts showed better response values toward all the investigated gases. Especially for n-butanol, methanol and isopropanol, they are more than four, two and three times of those of the pristine ZnO porous nanobelts, respectively. This suggests that the sensing performance of ZnO porous nanobelts is greatly improved by the doping of Pb. This result manifested the high sensing selectivity of the 0.61 at% Pb-doped ZnO porous nanobelts toward n-butanol, which could be ascribed to the particular active interfaces from the doped Pb ions at the surfaces, and also the synergistic effect between the molecular polarity of n-butanol and the polar surface provided by Pb. [41,52]. As shown in Figure 7b, the

long-term stability of the 0.61 at% Pb-doped ZnO porous nanobelts to 50 ppm n-butanol was examined during 100 days at 300 °C. For each measurement per 10 days, the relative response can be well-maintained without noticeable changes. The average of the relative response was 47.53 with a comparatively small variance of 0.324, which demonstrated a distinguished repeatability. This excellent stability is probably attributed to the fact that the sensing film is uniform, following the above in situ calcination process, and difficult to fall off from the alumina ceramic slice electrode. Additionally, the morphology of porous nanobelts, the key to obtain the excellent performance, was fundamentally preserved under the practical long-term use, due to the relative low working temperature of 300 °C, compared with the calcination temperature of 500 °C. Therefore, the n-butanol sensor based on the as-synthesized 0.61 at% Pb-doped ZnO porous nanobelts could be considered as a remarkable candidate for the actual application.

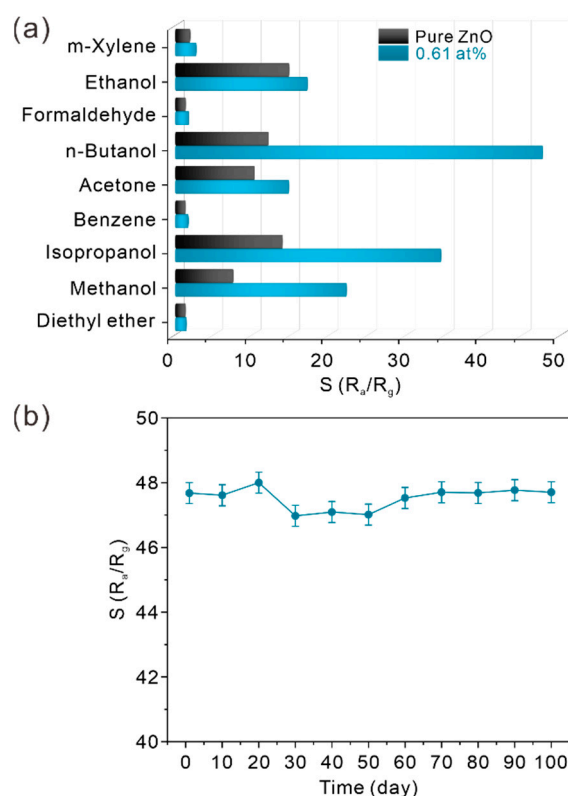


Figure 7. (a) The relative responses of pure ZnO porous nanobelts and 0.61 at% Pb-doped ZnO porous nanobelts toward 50 ppm of different VOCs at 300 °C, (b) the stability of 0.61 at% Pb-doped ZnO porous nanobelts to 50 ppm n-butanol during 100 days with variance.

3.3. Sensing Mechanism

The main principle of the sensing mechanism of MOS sensors is a phenomenon related to the process of chemical adsorption and desorption of gas molecules and the reaction between the gas molecules at the surfaces of sensing materials, which could be recorded and analyzed by measuring the change of the electrical resistance at the external circuit of the test system [53]. The gas sensor based on our as-synthesized 0.61 at% Pb-doped ZnO porous nanobelts should also abide by this principle, as shown by the sketch in Figure 8. When the sensor was exposed to the air atmosphere, the free oxygen molecules (O_2) in air were adsorbed on the sensing material and then successively converted into oxygen ions (O_2^-) by the capture of electrons from the sensing material. After the initial physical absorption, the oxygen ions continually ionized to the states of O^- and O^{2-} with the working temperature increasing, which established the electron depletion layer at the surface of the sensing materials [54]. Additionally, the energy barriers formed at the contact area among the nanobelts also enlarged the value of the resistance. Therefore, the

movement of the carriers in the sensor were greatly hindered, resulting in a relatively large resistivity. In addition, the resistivity of 0.61 at% Pb-doped ZnO porous nanobelts was much greater than that of the pristine ZnO porous nanobelts, due to the increased lattice defects and impurity ions caused by doped Pb, and was maintained regardless of the raising of the working temperature, as displayed in Figure S8. The electrical conductivity (σ) was defined as $\sigma = n\mu e$, where n was the concentration of the carriers, μ was the carrier mobility and e was the electron charge. The concentration of electrons was increased following the increment of oxygen vacancies by Pb doping, but, inversely, the resistance increased when the tendency of the decreasing carrier mobility was faster than that of increasing the electronic concentration. For the reason of the increased effective mass (m^*) near the Fermi level, the ionic impurity scattering, especially the partly incorporated Pb in the lattice and the microstructural complexity, the carrier mobility was dramatically decreased with the doping of Pb [19,21]. In short, the lattice scattering played a vital role here. Furthermore, the grain boundary, the principal factor of the lattice scattering, was enriched due to the high porosity and small grain sizes, which resulted in an enhanced influence of lattice scattering. Thus, the resistance increased even if the concentration of the electrons increased. The increased resistivity caused by the previously stated reasons lowered the baseline, ultimately, and enhanced the response of the as-prepared gas sensor [55].

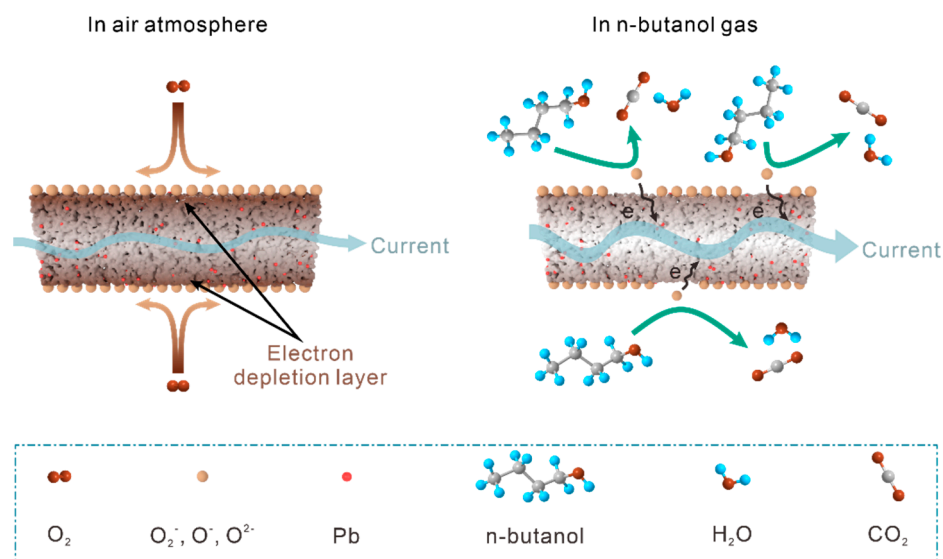


Figure 8. Possible sensing mechanism of porous Pb-doped ZnO nanobelts toward n-butanol.

When the testing chamber contained a certain amount of n-butanol by injection, the chemisorbed oxygen ions and their derivatives on the surface of the sensing materials would react with the gas molecules of the n-butanol, and then caused the backdonation of the trapped electrons to the depletion layers, resulting in the decrease in the sensor resistance due to the reduction in the range of depletion region and the height of the barriers between the nanobelts [56,57]. Meanwhile, the H₂O on the surface of the sensing film, one of the byproducts in the reaction described above, would further decrease the resistivity of the sensor [58]. Regarding the enhanced gas-sensing property of 0.61 at% Pb-doped ZnO porous nanobelts, it is worth noting that the gas-sensing process of pristine ZnO porous nanobelts was short of the sufficient adsorbed oxygen molecules and oxygen vacancies generated from the dopant of Pb. However, the effective sensitized region was diminished by the accumulation of the dopant, which contributed to the necessity to maintain a certain amount of the doped Pb.

4. Conclusions

In summary, porous Pb-doped ZnO nanobelts were successfully fabricated via a simply partial cation exchange method, followed by in situ thermal oxidation. The doped

Pb were uniformly distributed on the ZnO nanobelts and their doped amounts can be tuned in the process of the cation exchange reaction. The high porosity and uniformity of the doped Pb with enriched oxygen vacancies can result in an excellent gas-sensing performance with a long-term stability to n-butanol. At the optimal working temperature of 300 °C, the response time of 0.61 at% Pb-doped ZnO nanobelts toward 50 ppm n-butanol was as short as 5 s. Additionally, its relative response was up to 47.7, which was four times higher than that of pristine ZnO porous nanobelts. This work provides a novel approach to synthesize other uniform metal-doped ZnO porous nanobelts and is also believed to be further extended to prepare other doped metal oxide semiconductor nanostructures.

Supplementary Materials: The following supporting information can be downloaded at: <https://www.mdpi.com/article/10.3390/chemosensors10030096/s1>, Figure S1: (a) Structure of the as-fabricated sensing device, (b) Schematic setup of gas-sensing measurement; Figure S2: SEM images of 0.44 at% (a), 1.39 at% (b) and 2.01 at% (c) Pb²⁺-exchanged ZnSe precursor nanobelts, and 0.44 at% (d), 1.39 at% (e) and 2.01 at% (f) Pb-doped ZnO porous nanobelts; Figure S3: (a) TEM image of single Pb-doped precursor nanobelt, (b) its high magnified TEM, (c) its HAADF image and the corresponding elemental mapping patterns of (d) Zn, (e) Pb and (f) Se; Figure S4: EDX spectrum of the obtained Pb-doped ZnO porous nanobelts; Figure S5: High-resolution Zn 2p XPS spectra of pure ZnO porous nanobelts and 0.61 at% Pb-doped ZnO porous nanobelts; Figure S6: The real-time response curves of porous ZnO nanobelts doped with (a) 0 at%, (b) 0.44 at%, (c) 0.61 at%, (d) 1.39 at% and (e) 2.01 at% of Pb toward 50 ppm of n-butanol at different working temperature; Figure S7: (a) The real-time resistance response curve of 0.61 at% Pb-doped ZnO porous nanobelts toward 50 ppm of n-butanol at 300 °C, (b) The real-time resistance curve of pure ZnO porous nanobelts and 0.61 at% Pb-doped ZnO porous nanobelts toward different concentrations of n-butanol at 300 °C; Figure S8: The relationship between resistance and temperature of the sensing film fabricated with pure ZnO porous nanobelts and 0.61 at% Pb-doped ZnO porous nanobelts; Table S1: Structural parameters of as-synthesized samples analyzed at (100) from XRD data; Table S2: Fitting results of O 1s XPS spectrum of pure ZnO porous nanobelts and 0.61 at% Pb-doped ZnO porous nanobelts; Table S3: Relative response of various metal oxide nanostructures toward n-butanol, A reported in the literatures and the present work.

Author Contributions: Conceptualization, K.-G.Z. and Z.G.; formal analysis, K.-G.Z., Z.G. and T.-Y.Y.; investigation, K.-G.Z.; data curation, K.-G.Z. and T.-Y.Y.; writing—original draft preparation, K.-G.Z.; writing—review and editing, Z.G.; supervision, Z.G.; project administration, K.-G.Z.; funding acquisition, Z.G. All authors have read and agreed to the published version of the manuscript.

Funding: This work was supported by the National Natural Science Foundation of China (61774159 and 22001001), Anhui Provincial Natural Science Foundation (2008085QF320).

Institutional Review Board Statement: Not applicable.

Informed Consent Statement: Not applicable.

Data Availability Statement: Not applicable.

Conflicts of Interest: The authors declare no conflict of interest.

References

1. Zhao, Y.; Zhang, W.; Yang, B.; Liu, J.; Chen, X.; Wang, X.; Yang, C. Gas-sensing enhancement methods for hydrothermal synthesized SnO₂-based sensors. *Nanotechnology* **2017**, *28*, 452002. [[CrossRef](#)]
2. Yuan, Z.; Han, E.; Meng, F.; Zuo, K. Detection and Identification of Volatile Organic Compounds Based on Temperature-Modulated ZnO Sensors. *IEEE Trans. Instrum. Meas.* **2019**, *69*, 4533–4544. [[CrossRef](#)]
3. Zhao, Z.; Tian, J.; Sang, Y.; Cabot, A.; Liu, H. Structure, synthesis, and applications of TiO₂ nanobelts. *Adv. Mater.* **2015**, *27*, 2557–2582. [[CrossRef](#)] [[PubMed](#)]
4. Jeong, S.Y.; Kim, J.S.; Lee, J.H. Rational Design of Semiconductor-Based Chemiresistors and their Libraries for Next-Generation Artificial Olfaction. *Adv. Mater.* **2020**, *32*, 2002075. [[CrossRef](#)]
5. Bai, S.; Tian, K.; Han, N.; Guo, J.; Luo, R.; Li, D.; Chen, A. A novel rGO-decorated ZnO/BiVO₄ heterojunction for the enhancement of NO₂ sensing properties. *Inorg. Chem. Front.* **2020**, *7*, 1026–1033. [[CrossRef](#)]
6. An, D.; Liu, N.; Zhang, H.; Sun, Q.; Li, C.; Li, Y.; Zhang, Q.; Lu, Y. Enhanced n-butanol sensing performance of SnO₂-based gas sensors by doping In₂O₃ via co-precipitation method. *Sens. Actuators B Chem.* **2021**, *340*, 129944. [[CrossRef](#)]

7. Nakayama, R.; Maesato, M.; Lim, G.; Arita, M.; Kitagawa, H. Heavy Hydrogen Doping into ZnO and the H/D Isotope Effect. *J. Am. Chem. Soc.* **2021**, *143*, 6616–6621. [[CrossRef](#)]
8. Zunger, A.; Malyi, O.I. Understanding Doping of Quantum Materials. *Chem. Rev.* **2021**, *121*, 3031–3060. [[CrossRef](#)]
9. Montazeri, A.; Jamali-Sheini, F. Enhanced ethanol gas-sensing performance of Pb-doped In₂O₃ nanostructures prepared by sonochemical method. *Sens. Actuators B Chem.* **2017**, *242*, 778–791. [[CrossRef](#)]
10. Yousefi, R.; Zak, A.K.; Jamali-Sheini, F.; Huang, N.M.; Basirun, W.J.; Sookhakian, M. Synthesis and characterization of single crystal PbO nanoparticles in a gelatin medium. *Ceram. Int.* **2014**, *40*, 11699–11703. [[CrossRef](#)]
11. Rao, A.; Long, H.; Harley-Trochimczyk, A.; Pham, T.; Zettl, A.; Carraro, C.; Maboudian, R. In Situ Localized Growth of Ordered Metal Oxide Hollow Sphere Array on Microheater Platform for Sensitive, Ultra-Fast Gas Sensing. *ACS Appl. Mater. Interfaces* **2017**, *9*, 2634–2641. [[CrossRef](#)] [[PubMed](#)]
12. Gu, J.; Zhang, B.; Li, Y.; Xu, X.; Sun, G.; Cao, J.; Wang, Y. Synthesis of spindle-like Co-doped LaFeO₃ porous microstructure for high performance n-butanol sensor. *Sens. Actuators B Chem.* **2021**, *343*, 130125. [[CrossRef](#)]
13. Guo, Z.; Li, M.-Q.; Liu, J.-H.; Huang, X.-J. Cation Exchange Synthesis and Unusual Resistive Switching Behaviors of Ag₂Se Nanobelts. *Small* **2015**, *11*, 6285–6294. [[CrossRef](#)] [[PubMed](#)]
14. Kang, P.; Zheng, K.-G.; Wang, Z.; Chen, L.; Guo, Z. Cation-exchange synthesis of PbSe/ZnSe hetero-nanobelts with enhanced near-infrared photoelectronic performance. *Nanotechnology* **2021**, *32*, 335504. [[CrossRef](#)] [[PubMed](#)]
15. Jin, X.-B.; Li, Y.-X.; Su, Y.; Guo, Z.; Gu, C.-P.; Huang, J.-R.; Meng, F.-L.; Huang, X.-J.; Li, M.-Q.; Liu, J.-H. Porous and single-crystalline ZnO nanobelts: Fabrication with annealing precursor nanobelts, and gas-sensing and optoelectronic performance. *Nanotechnology* **2016**, *27*, 355702. [[CrossRef](#)] [[PubMed](#)]
16. Tian, H.; Fan, H.; Li, M.; Ma, L. Zeolitic Imidazolate Framework Coated ZnO Nanorods as Molecular Sieving to Improve Selectivity of Formaldehyde Gas Sensor. *ACS Sens.* **2015**, *1*, 243–250. [[CrossRef](#)]
17. Pavithra, M.; Raj, M.J. Influence of ultrasonication time on solar light irradiated photocatalytic dye degradability and antibacterial activity of Pb doped ZnO nanocomposites. *Ceram. Int.* **2021**, *47*, 32324–32331. [[CrossRef](#)]
18. Yang, D.; Su, X.; Yan, Y.; Hu, T.; Xie, H.; He, J.; Uher, C.; Kanatzidis, M.G.; Tang, X. Manipulating the Combustion Wave during Self-Propagating Synthesis for High Thermoelectric Performance of Layered Oxychalcogenide Bi_{1-x}Pb_xCuSeO. *Chem. Mater.* **2016**, *28*, 4628–4640. [[CrossRef](#)]
19. Li, X.B.; Ma, S.Y.; Li, F.M.; Yang, F.C.; Liu, J.; Zhang, X.L.; Wang, X. Blue-green and red luminescence from non-polar ZnO:Pb films. *Appl. Surf. Sci.* **2013**, *270*, 467–472. [[CrossRef](#)]
20. Aboud, A.A.; Shaban, M.; Revaprasadu, N. Effect of Cu, Ni and Pb doping on the photo-electrochemical activity of ZnO thin films. *RSC Adv.* **2019**, *9*, 7729–7736. [[CrossRef](#)]
21. Yin, Z.; Liu, Z.; Yu, Y.; Zhang, C.; Chen, P.; Zhao, J.; He, P.; Guo, X. Synergistically Optimized Electron and Phonon Transport of Polycrystalline BiCuSeO via Pb and Yb Co-Doping. *ACS Appl. Mater. Inter.* **2021**, *13*, 57638–57645. [[CrossRef](#)] [[PubMed](#)]
22. Liu, W.; Gu, D.; Li, X. Ultrasensitive NO₂ Detection Utilizing Mesoporous ZnSe/ZnO Heterojunction-Based Chemiresistive-Type Sensors. *ACS Appl. Mater. Interf.* **2019**, *11*, 29029–29040. [[CrossRef](#)] [[PubMed](#)]
23. Xing, C.; Chen, X.; Huang, W.; Song, Y.; Li, J.; Chen, S.; Zhou, Y.; Dong, B.; Fan, D.; Zhu, X.; et al. Two-Dimensional Lead Monoxide: Facile Liquid Phase Exfoliation, Excellent Photoresponse Performance, and Theoretical Investigation. *ACS Photon.* **2018**, *5*, 5055–5067. [[CrossRef](#)]
24. Kumar, P.; Liu, J.; Ranjan, P.; Hu, Y.; Yamijala, S.S.; Pati, S.K.; Cheng, G.J. Alpha Lead Oxide (alpha-PbO): A New 2D Material with Visible Light Sensitivity. *Small* **2018**, *14*, 1703346. [[CrossRef](#)]
25. Liu, X.; Min, L.; Yu, X.; Zhou, Z.; Sha, L.; Zhang, S. Changes of photoelectrocatalytic, electrocatalytic and pollutant degradation properties during the growth of β-PbO₂ into black titanium oxide nanoarrays. *Chem. Eng. J.* **2021**, *417*, 127996. [[CrossRef](#)]
26. Jiang, W.; Wang, S.; Liu, J.; Zheng, H.; Gu, Y.; Li, W.; Shi, H.; Li, S.; Zhong, X.; Wang, J. Lattice oxygen of PbO₂ induces crystal facet dependent electrochemical ozone production. *J. Mater. Chem. A* **2021**, *9*, 9010–9017. [[CrossRef](#)]
27. Zhang, D.; Yang, Z.; Wu, Z.; Dong, G. Metal-organic frameworks-derived hollow zinc oxide/cobalt oxide nanoheterostructure for highly sensitive acetone sensing. *Sens. Actuators B Chem.* **2018**, *283*, 42–51. [[CrossRef](#)]
28. Jiang, W.; Low, J.; Mao, K.; Duan, D.; Chen, S.; Liu, W.; Pao, C.-W.; Ma, J.; Sang, S.; Shu, C. Pd-Modified ZnO-Au Enabling Alkoxy Intermediates Formation and Dehydrogenation for Photocatalytic Conversion of Methane to Ethylene. *J. Am. Chem. Soc.* **2021**, *143*, 269–278. [[CrossRef](#)]
29. Wang, Z.; Gao, S.; Fei, T.; Liu, S.; Zhang, T. Construction of ZnO/SnO₂ Heterostructure on Reduced Graphene Oxide for Enhanced Nitrogen Dioxide Sensitive Performances at Room Temperature. *ACS Sens.* **2019**, *4*, 2048–2057. [[CrossRef](#)]
30. Yan, W.; Xu, H.; Ling, M.; Zhou, S.; Qiu, T.; Deng, Y.; Zhao, Z.; Zhang, E. MOF-Derived Porous Hollow Co₃O₄@ZnO Cages for High-Performance MEMS Trimethylamine Sensors. *ACS Sens.* **2021**, *6*, 2613–2621. [[CrossRef](#)]
31. Huang, B.; Zhang, Z.; Zhao, C.; Cairang, L.; Bai, J.; Zhang, Y.; Xie, E. Enhanced gas-sensing performance of ZnO@In₂O₃ core@shell nanofibers prepared by coaxial electrospinning. *Sens. Actuators B Chem.* **2018**, *255*, 2248–2257. [[CrossRef](#)]
32. Liu, W.; Xu, L.; Sheng, K.; Chen, C.; Zhou, X.; Dong, B.; Bai, X.; Zhang, S.; Lu, G.; Song, H. APTES-functionalized thin-walled porous WO₃ nanotubes for highly selective sensing of NO₂ in a polluted environment. *J. Mater. Chem. A* **2018**, *6*, 10976–10989. [[CrossRef](#)]
33. Li, L.; He, S.; Liu, M.; Zhang, C.; Chen, W. Three-Dimensional Mesoporous Graphene Aerogel-Supported SnO₂ Nanocrystals for High-Performance NO₂ Gas Sensing at Low Temperature. *Anal. Chem.* **2015**, *87*, 1638–1645. [[CrossRef](#)] [[PubMed](#)]

34. Chen, D.; Zhang, K.; Zhou, H.; Fan, G.; Wang, Y.; Li, G.; Hu, R. A wireless-electrodeless quartz crystal microbalance with dissipation DMMP sensor. *Sens. Actuators B Chem.* **2018**, *261*, 408–417. [[CrossRef](#)]
35. Koo, W.-T.; Choi, S.-J.; Kim, S.-J.; Jang, J.-S.; Tuller, H.L.; Kim, I.-D. Heterogeneous Sensitization of Metal–Organic Framework Driven Metal@Metal Oxide Complex Catalysts on an Oxide Nanofiber Scaffold Toward Superior Gas Sensors. *J. Am. Chem. Soc.* **2016**, *138*, 13431–13437. [[CrossRef](#)]
36. Swaminathan, N.; Henning, A.; Jurca, T.; Hayon, J.; Shalev, G.; Rosenwaks, Y. Effect of varying chain length of n-alcohols and n-alkanes detected with electrostatically-formed nanowire sensor. *Sens. Actuators B Chem.* **2017**, *248*, 240–246. [[CrossRef](#)]
37. Chen, M.; Zhang, Y.; Zhang, J.; Li, K.; Lv, T.; Shen, K.; Zhu, Z.; Liu, Q. Facile lotus-leaf-templated synthesis and enhanced xylene gas sensing properties of Ag-LaFeO₃ nanoparticles. *J. Mater. Chem. C* **2018**, *6*, 6138–6145. [[CrossRef](#)]
38. Wang, Y.; Zeng, Y.; Wang, L.; Lou, Z.; Qiao, L.; Tian, H.; Zheng, W. Ultrathin nanorod-assembled SnO₂ hollow cubes for high sensitive n-butanol detection. *Sens. Actuators B Chem.* **2018**, *283*, 693–704. [[CrossRef](#)]
39. Liu, F.; Huang, G.; Wang, X.; Xie, X.; Xu, G.; Lu, G.; He, X.; Tian, J.; Cui, H. High response and selectivity of single crystalline ZnO nanorods modified by In₂O₃ nanoparticles for n-butanol gas sensing. *Sens. Actuators B Chem.* **2019**, *277*, 144–151. [[CrossRef](#)]
40. Yang, W.; Xiao, X.; Fang, B.; Deng, H. Nanorods-assembled ZnO microflower as a powerful channel for n-butanol sensing. *J. Alloys Compd.* **2021**, *860*, 158410. [[CrossRef](#)]
41. Hoppe, M.; Ababii, N.; Postica, V.; Lupan, O.; Polonskyi, O.; Schütt, F.; Kaps, S.; Sukhodub, L.F.; Sontea, V.; Strunskus, T.; et al. (CuO-Cu₂O)/ZnO:Al heterojunctions for volatile organic compound detection. *Sens. Actuators B Chem.* **2018**, *255*, 1362–1375. [[CrossRef](#)]
42. Zhao, R.; Wei, Q.; Ran, Y.; Kong, Y.; Ma, D.; Su, L.; Yao, L.; Wang, Y. One-dimensional In₂O₃ nanorods as sensing material for ppb-level n-butanol detection. *Nanotechnology* **2021**, *32*, 375501. [[CrossRef](#)] [[PubMed](#)]
43. Li, W.; Ren, Y.; Guo, Y. ZrO₂/ZnO nanocomposite materials for chemiresistive butanol sensors. *Sens. Actuators B Chem.* **2020**, *308*, 127658. [[CrossRef](#)]
44. Wang, S.; Gao, X.; Yang, J.; Zhu, Z.; Zhang, H.; Wang, Y. Synthesis and gas sensor application of ZnFe₂O₄-ZnO composite hollow microspheres. *RSC Adv.* **2014**, *4*, 57967–57974. [[CrossRef](#)]
45. Wang, M.; Shen, Z.; Zhao, X.; Duanmu, F.; Yu, H.; Ji, H. Rational shape control of porous Co₃O₄ assemblies derived from MOF and their structural effects on n-butanol sensing. *J. Hazard. Mater.* **2019**, *371*, 352–361. [[CrossRef](#)]
46. Bai, J.; Li, Y.; Liu, Y.; Wang, H.; Liu, F.; Liu, F.; Sun, P.; Yan, X.; Lu, G. Au₃₉Rh₆₁ Alloy Nanocrystal-Decorated W₁₈O₄₉ for Enhanced Detection of n-Butanol. *ACS Sens.* **2019**, *4*, 2662–2670. [[CrossRef](#)]
47. Xu, Y.; Zheng, L.; Yang, C.; Zheng, W.; Liu, X.; Zhang, J. Chemiresistive sensors based on core-shell ZnO@TiO₂ nanorods designed by atomic layer deposition for n-butanol detection. *Sens. Actuators B Chem.* **2020**, *310*, 127846. [[CrossRef](#)]
48. Lv, L.; Cheng, P.; Wang, Y.; Xu, L.; Zhang, B.; Lv, C.; Ma, J.; Zhang, Y. Sb-doped three-dimensional ZnFe₂O₄ macroporous spheres for N-butanol chemiresistive gas sensors. *Sens. Actuators B Chem.* **2020**, *320*, 128384. [[CrossRef](#)]
49. Wang, Y.; Zhang, B.; Liu, J.; Yang, Q.; Cui, X.; Gao, Y.; Chuai, X.; Liu, F.; Sun, P.; Liang, X.; et al. Au-loaded mesoporous WO₃: Preparation and n-butanol sensing performances. *Sens. Actuators B Chem.* **2016**, *236*, 67–76. [[CrossRef](#)]
50. He, P.; Fu, H.; Yang, X.; Xiong, S.; Han, D.; An, X. Variable gas sensing performance towards different volatile organic compounds caused by integration types of ZnS on In₂O₃ hollow spheres. *Sens. Actuators B Chem.* **2021**, *345*, 130316. [[CrossRef](#)]
51. Dang, F.; Wang, Y.; Gao, J.; Xu, L.; Cheng, P.; Lv, L.; Zhang, B.; Li, X.; Wang, C. Hierarchical flower-like NiCo₂O₄ applied in n-butanol detection at low temperature. *Sens. Actuators B Chem.* **2020**, *320*, 128577. [[CrossRef](#)]
52. Cho, S.Y.; Yoo, H.W.; Kim, J.Y.; Jung, W.B.; Jin, M.L.; Kim, J.S.; Jeon, H.-J.; Jung, H.-T. High-Resolution p-Type Metal Oxide Semiconductor Nanowire Array as an Ultrasensitive Sensor for Volatile Organic Compounds. *Nano Lett.* **2016**, *16*, 4508–4515. [[CrossRef](#)] [[PubMed](#)]
53. Shehada, N.; Brönstrup, G.; Funke, K.; Christiansen, S.; Leja, M.; Haick, H. Ultrasensitive Silicon Nanowire for Real-World Gas Sensing: Noninvasive Diagnosis of Cancer from Breath Volatolome. *Nano Lett.* **2014**, *15*, 1288–1295. [[CrossRef](#)]
54. Alali, K.T.; Liu, J.; Liu, Q.; Li, R.; Zhang, H.; Aljebawi, K.; Liu, P.; Wang, J. Enhanced acetone gas sensing response of ZnO/ZnCo₂O₄ nanotubes synthesized by single capillary electrospinning technology. *Sens. Actuators B Chem.* **2017**, *252*, 511–522. [[CrossRef](#)]
55. Wei, D.; Huang, Z.; Wang, L.; Chuai, X.; Zhang, S.; Lu, G. Hydrothermal synthesis of Ce-doped hierarchical flower-like In₂O₃ microspheres and their excellent gas-sensing properties. *Sens. Actuators B Chem.* **2018**, *255*, 1211–1219. [[CrossRef](#)]
56. Spagnoli, E.; Krik, S.; Fabbri, B.; Valt, M.; Ardit, M.; Gaiardo, A.; Vanzetti, L.; Della Ciana, M.; Cristino, V.; Vola, G.; et al. Development and characterization of WO₃ nanoflakes for selective ethanol sensing. *Sens. Actuators B Chem.* **2021**, *347*, 130593. [[CrossRef](#)]
57. Masoumi, S.; Shokrani, M.; Aghili, S.; Hossein-Babaei, F. Zinc oxide-based direct thermoelectric gas sensor for the detection of volatile organic compounds in air. *Sens. Actuators B Chem.* **2019**, *294*, 245–252. [[CrossRef](#)]
58. Postica, V.; Lupan, O.; Gapeeva, A.; Hansen, L.; Khaledialidusti, R.; Mishra, A.K.; Drewes, J.; Kersten, H.; Faupel, F.; Adelung, R.; et al. Improved Long-Term Stability and Reduced Humidity Effect in Gas Sensing: SiO₂ Ultra-Thin Layered ZnO Columnar Films. *Adv. Mater. Technol.* **2021**, *6*, 2001137. [[CrossRef](#)]